Advances in Water Resources 127 (2019) 1–12

Contents lists available at ScienceDirect

Advances in Water Resources

journal homepage: www.elsevier.com/locate/advwatres

Hydraulic conductivity and porosity heterogeneity controls on environmental performance metrics: Implications in probabilistic risk analysis

Arianna Libera[a,*], Christopher V. Henri[b], Felipe P.J. de Barros[a]

[a] Sonny Astani Dept. of Civil and Environmental Engineering, University of Southern California, Los Angeles, CA, USA
[b] Dept. of Land, Air and Water Resources, University of California, Davis, CA, USA

A B S T R A C T

Heterogeneities in natural porous formations, mainly manifested through the hydraulic conductivity (K) and, to a lesser degree, the porosity (ϕ), largely control subsurface flow and solute transport. The influence of the heterogeneous structure of K on transport processes has been widely studied, whereas less attention is dedicated to the joint heterogeneity of conductivity and porosity fields. Our study employs Monte Carlo simulations to investigate the coupled effect of $K-\phi$ spatial variability on the transport behavior (and uncertainty) of conservative and reactive plumes within a 3D aquifer domain. We explore multiple scenarios, characterized by different levels of heterogeneity of the geological properties, and compare the computational results from the joint $K-\phi$ heterogeneous system with the results originating from generally adopted constant ϕ conditions. In our study, the spatially variable $K-\phi$ fields are positively correlated. We statistically analyze key Environmental Performance Metrics: first arrival times and peak mass fluxes for non-reactive species and increased lifetime cancer risk for reactive chlorinated solvents. The conservative transport simulations show that considering coupled $K-\phi$ fields decreases the plume dispersion, increases both the first arrival times of solutes and the peak mass fluxes at the observation planes. A positive correlation between aquifer connectivity and peak mass fluxes is identified for both homogeneous and heterogeneous ϕ. Our conservative transport results indicate that the relevance of ϕ variability can depend on the metric of interest, the control plane-source distance as well as the level of heterogeneity of the conductivity field. The analysis on reactive transport shows that ϕ variability only slightly affects the mean increased lifetime cancer risk at the control planes but leads to a considerable reduction of the cancer risk uncertainty. We also see that the sensitivity of cancer risk towards ϕ heterogeneity can be influenced by the level of variability of the conductivity field, the source-to-control plane distance, but is not affected by the manner in which the contaminant concentration is computed.

1. Introduction

It is well established that heterogeneities in natural porous formations largely control subsurface groundwater flow and contaminant transport. These heterogeneities are mainly manifested through the hydraulic conductivity (K) and, to a lesser degree, the porosity (ϕ). The influence of the heterogeneous K-field on flow and solute transport processes has been widely studied (see Rubin, 2003, and references therein), whereas less attention is dedicated to the effect of heterogeneous ϕ. Hydraulic conductivity is commonly modeled as a random space function (RSF) in the stochastic hydrogeology community because of its erratic spatial variability and the large uncertainty associated with incomplete site characterization (Dagan, 1986; Gelhar, 1986). ϕ variability is commonly regarded as a secondary factor when compared to K heterogeneity. Indeed, most studies in the field of stochastic hydrogeology assume that aquifers are characterized by spatially heterogeneous K and homogeneous ϕ. This is partially justified because K can vary in space by 3–4 orders of magnitude within small distances while the range of variability of ϕ in unconsolidated granular aquifers is generally between 0.1 and 0.55 (Atkins and McBride, 1992; Freeze and Cherry, 1979; Hu et al., 2009).

Because of the limited availability of K and ϕ measurements, it is difficult to establish a clear correlation between the two geological properties. However, in specific formations, a level of correlation is likely to be present (Hassan et al., 1998). The literature presents different studies exploring the relationship between K and ϕ. Archie (1950) and Doyen (1988) found positive correlation between the variables. Additionally, different authors investigating the estimation of K from ϕ and other measurable parameters (e.g. grain size, pore surface area, pore dimension) established positive correlation between K and ϕ for different types of soil (e.g., Aimrun et al., 2004; Fallico, 2014; Franzmeier, 1991; Nelson et al., 1994; Panda and Lake, 1994; Riva et al., 2014; Scholz et al., 2012). Among them, Nelson et al. (1994) analyzed different models to predict permeability in sedimentary rocks and concluded that, in most cases, the permeability is related to a power of ϕ and to the square of a measure of surface area or a characteristic length. It is typically assumed that K and ϕ are positively correlated in unconsolidated aquifers (Hu et al., 2009), however some studies observed negative correlation

* Corresponding author.
E-mail address: libera@usc.edu (A. Libera).

https://doi.org/10.1016/j.advwatres.2019.03.002
Received 6 November 2018; Received in revised form 8 February 2019; Accepted 7 March 2019
Available online 8 March 2019

between the two properties under specific packing arrangements and grain size distributions (Morin, 2006).

Only a small number of studies investigated the effects of spatially variable ϕ fields on transport predictions. Among them, Warren et al. (1964) did not consider a correlation between K and ϕ and concluded that the impact of ϕ variations on macroscopic dispersion is minor with respect to the effect of K variability. Lin (1977) analyzed various porosity functions to represent ϕ spatial variability in porous media and indicated that the solute concentration predictions are within 15% of the concentration resulting from an average ϕ when a linear or slightly curved equation that expresses porosity as a function of the spatial coordinate, is employed. The author pointed out that the discrepancies of solute concentrations become very substantial as the deviation of the porosity function from linearity increases. A few numerical modeling studies (e.g., Hassan, 2001; Hassan et al., 1998; Hu et al., 2009) showed that the consideration of correlated heterogeneous K and ϕ fields significantly impacts contaminant transport for two-dimensional domains. Hassan et al. (1998) indicated that a positive correlation between ϕ and K decreases dispersion whereas a negative correlation enhances plume spreading, particularly along the longitudinal direction. Hassan et al. (1998) also considered reactive transport and indicated that reaction rates impact the relative importance of ϕ variability on concentration estimation, which appears to be amplified in the presence of slow reactions. Along the same line of work, Hassan (2001) highlighted that ϕ spatial variability, correlated to heterogeneous K, impacts the longitudinal velocity covariance as well as its cross covariance with the head and the log-conductivity ($Y \equiv \ln[K]$) fields. Riva et al. (2006) studied the influence of K heterogeneities on solute transport with constant effective ϕ, and later expanded their analysis in Riva et al. (2008), where both K and ϕ were considered random variables. Riva et al. (2008) highlighted that considering the spatial distribution of ϕ is fundamental to mimic the early arrival of breakthrough curves (BTCs). The studies of Riva et al. (2008, 2006) showed that the site description of transport processes highly profits from the incorporation of the spatial variability of the ϕ field.

In light of the mentioned findings, the influence of heterogeneous K coupled with spatially variable ϕ fields, especially when the two properties are correlated, as shown in most cases, should be further investigated to increase the reliability of contaminant transport and associated human health risk predictions. In this context, our work aims to study the significance of spatial variability in the porous medium's ϕ to conservative and reactive solute transport predictions in the context of probabilistic risk analysis. Through the use of stochastic numerical simulations we systematically illustrate the impact of $K-\phi$ spatial variability on key *Environmental Performance Metrics* (EPMs) such as solute arrival times, peak mass fluxes, increased lifetime cancer risk and corresponding uncertainties at environmentally sensitive locations. For our illustrations, we consider three-dimensional (3D) heterogeneous aquifer systems. In particular, the objectives of this work are twofold. First, we systematically investigate the coupled influence of ϕ and K heterogeneity on the statistical characterization of non-reactive transport. Second, within an application-oriented context, we show the implications of these coupled effects when estimating adverse human health effects (e.g. cancer risk) due to exposure to chlorinated solvents in groundwater. Through extensive stochastic computational analysis, we explore different scenarios that, to the best of our knowledge, have not been investigated, with the goal of identifying conditions where the role of spatially variable ϕ, correlated to heterogeneous K, is relevant. Our analysis simulates contaminant transport through an unconsolidated sandy aquifer where, given the likelihood (Hassan, 2001; Hu et al., 2009; Luijendijk and Gleeson, 2015), positive $K-\phi$ correlation is adopted, together with different levels of heterogeneity of the K system. Our study addresses fundamental questions such as: is the uncertainty associated with transport in the subsurface increased or decreased when variable ϕ fields are considered? Does the relative importance of variable ϕ depend on the level of heterogeneity of the K-field? What is the impact of this joint heterogeneity on the flow connectivity structure of the aquifer? How are the effects of heterogeneity propagated to decision making metrics such as human health risk?

The paper is structured as follows. We present the problem under investigation in Section 2. In Section 3, we illustrate the methodology employed in our study and provide details on the computational implementation. Next, Section 4 is devoted to the analysis of the results for conservative tracers (Section 4.1) and reactive contaminants (Section 4.2). We finally summarize our study and outline the key findings in Section 5.

2. Problem statement

In this work we consider a contaminated, fully saturated 3D heterogeneous aquifer whose Cartesian coordinate system is indicated by $\mathbf{x} = (x, y, z)$. We are interested in understanding the impact of heterogeneity, stemming from both K and ϕ, on a series of EPMs (de Barros et al., 2012).

Let Ω denote a generic EPM. For example, Ω can represent solute arrival times or solute peak concentrations at an environmentally sensitive location. If the contaminant is toxic, then Ω can denote, for instance, an adverse health effect. Due to incomplete characterization of the subsurface, hydrogeological properties such as K and ϕ are modeled as spatially random. As a consequence, the quantity Ω is subject to uncertainty and quantified through its statistical moments, such as its mean $\langle\Omega\rangle$ (where the angled brackets denote ensemble expectation), its variance σ^2_Ω, and its probability density function (PDF) $p(\Omega)$ or cumulative density function (CDF) $P(\Omega)$.

We are primarily interested in analyzing the effect of $K-\phi$ variability on different EPMs with the goal of: (a) improving our fundamental understanding of the significance of these variabilities to contaminant transport and (b) exploring how the latter variabilities propagate to decision making metrics relevant to human health risk analysis. In this study we perform both conservative and reactive contaminant transport simulations and select the specific EPMs indicated below:

- We statistically analyze the first arrival times and peak mass fluxes through control planes (CPs) resulting from conservative tracer simulations. The first arrival time is defined as the time of arrival of 5% of the initial injected mass (i.e., $t_{5\%}$) at the CP of interest. An accurate detection of $t_{5\%}$ is of fundamental importance for risk and water entities in charge of accurately planning aquifer remediation, risk analysis and managing water resources. Moreover, peak mass fluxes at an environmentally sensitive location can be viewed as an indicator of the risks associated with groundwater contamination and can also serve as a proxy for dilution (Fiori, 2001).
- We then explore the increased lifetime cancer risk estimates associated with chronic exposure to chlorinated solvents that are the reactive contaminants of interest in our study. The latter metric is of fundamental importance for public health authorities and its quantification provides useful insights for risk and remediation experts in order to characterize risk of real-life operations.

2.1. K − ϕ model

The interdependence between the heterogeneous K and ϕ fields is largely uncertain as explained in Section 1. However a positive correlation is likely to be present in unconsolidated sandy aquifers (e.g., Hu et al., 2009; Luijendijk and Gleeson, 2015). With the goal of systematically exploring the influence of spatially variable ϕ and K on the EPMs described before, we model our aquifer system as being characterized by (a) spatially heterogeneous K and homogeneous ϕ, and (b) spatially heterogeneous K correlated to spatially heterogeneous ϕ.

In order to illustrate the possible relationship between K and ϕ data, we report in Fig. 1 permeability (k) and ϕ data for different formations. Data presented in purple refer to experimental measurements of a sequence of seven samples of Fountainebleau sandstone (Doyen, 1988),

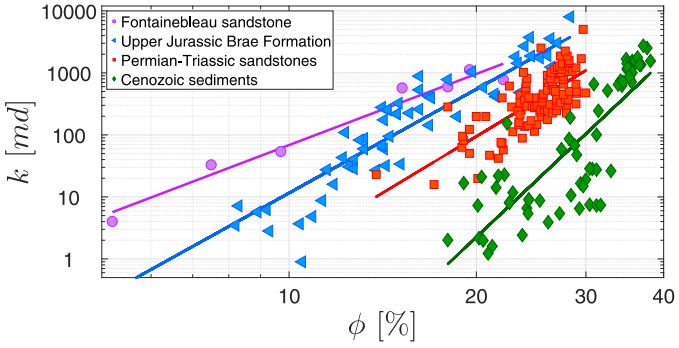

Fig. 1. Log-log plot of permeability (k) as a function of porosity (ϕ) for different formations showing a positive correlation trend: Fontainebleau sandstone data from the study of Doyen (1988) in purple, Upper Jurassic Brae Formation, East Brae field Offshore United Kingdom, North Sea (Grau, 2000; Nelson, 2004) in blue light, Permian-Triassic sandstones, Ivishak Formation, Sadlerochit Group, Prudhoe Bay Field, Alaska (Atkinson et al., 1990; Nelson, 2004) in red, core-plug samples of Cenozoic sediments from geothermal well AST-02 in the Roer Valley Graben, southern Netherlands (Luijendijk and Gleeson, 2015) in green. (For interpretation of the references to colour in this figure legend, the reader is referred to the web version of this article.)

in blue light we show samples from a turbidite reservoir of Late Jurassic age located in the North Sea (Grau, 2000; Nelson, 2004). Furthermore, data from Permian-Triassic sandstones from Prudhoe Bay Field, Alaska, USA, are pictured in red (Atkinson et al., 1990; Nelson, 2004), whereas core-plug samples of Cenozoic sediments from the southern Netherlands (Luijendijk and Gleeson, 2015) are shown in green in Fig. 1. We recall that permeability, k, is directly proportional to K through $K = k\rho g/\mu$ (Bear, 1979), where ρ indicates water density (1000 g/m^3), g is the gravity acceleration (9.8 m/s^2) and μ is the dynamic viscosity of water. We adopted a value of μ equal to 8.84×10^{-4} Pa s, i.e., a temperature of 25° C. Note that k in Fig. 1 is expressed in md, 1 md being equivalent to 9.87×10^{-16} m^2. Interpolation of ϕ and k data of Fig. 1 suggests a positive correlation for all the formations presented.

In our work we consider a porous formation composed by unconsolidated sandy material and we assume positive correlation between the heterogeneous K and ϕ fields. For the purpose of illustration we estimate that the relationship among ϕ and K can be described by the well-known Kozeny–Carman (KC) empirical equation (Carman, 1937; 1956; Kozeny, 1927):

$$K = \frac{\rho g}{\mu} \frac{\phi^3}{(1-\phi)^2} \frac{d_e^2}{180}, \tag{1}$$

where d_e indicates the representative diameter of grains and the remaining parameters have been previously defined. The literature presents different interpretations for d_e (e.g., Koltermann and Gorelick, 1995) and we assume that the latter corresponds to d_{10}, i.e., the grain diameter at which 10% of the particles are smaller, in our study.

The KC equation has been proven effective in predicting the permeability of sand from porosity data and generally gives good predictions of hydraulic conductivity when the value of d_{10} is within the range 0.1–3 mm (Barahona-Palomo et al., 2011). The KC formula has been employed in different studies (e.g., Barahona-Palomo et al., 2011; Bianchi and Zheng, 2016; Luijendijk and Gleeson, 2015; Odong, 2007; Riva et al., 2010). Luijendijk and Gleeson (2015) concluded that permeability of pure sand can be predicted with high confidence ($R^2 \geq 0.9$) using the KC equation. Bianchi and Zheng (2016) used the relationship to first estimate the K values of lithofacies during three-dimensional stochastic flow and transport modeling at the MADE site. Odong (2007) tested the reliability of different empirical formulas to estimate the hydraulic conductivity of unconsolidated aquifers by particle size analysis and identified the KC equation as the overall best estimator. Other authors, as Barr (2005) and Carrier III (2003), also encouraged the use of the KC formula.

We point out that the scope of our work is to explore the influence of possible combinations of spatially variable ϕ and K on the transport of tracers and reactive contaminants. Our goal is to assess the impact of neglecting the joint variability of ϕ and K on the probabilistic assessment of the risks associated with groundwater contamination. The estimation of the ϕ fields from K through the KC relationship is chosen for the purpose of illustration and given its suitability to unconsolidated sandy aquifers, shown in different studies (e.g., Hu et al., 2009; Luijendijk and Gleeson, 2015). However, we point out the KC equation implies a full positive correlation between ϕ and K but, in reality, the correlation between the two hydrogeological properties is partial and nonlinear (e.g., Hu et al., 2009). Therefore, the KC equation can be a reliable predictor of K from ϕ only for some cases and is used in this work for the purpose of illustration. We emphasize that other empirical relationships between ϕ and K, which are site-specific, for example obtained through borehole geophysics techniques, can be utilized within the methodological framework adopted in this study.

2.2. Flow and transport model

Groundwater flow A steady state uniform-in-the mean base flow (q_0) takes place along the longitudinal x-direction within the 3D heterogeneous aquifer in the absence of sinks and sources. Constant head conditions are established at the west and east boundaries and no-flow conditions are set at the remaining boundaries. The steady-state groundwater flow is governed by the following partial differential equation:

$$\nabla \cdot \mathbf{q}(\mathbf{x}) = 0, \tag{2}$$

with

$$\mathbf{q}(\mathbf{x}) = -K(\mathbf{x})\nabla h(\mathbf{x}), \tag{3}$$

where $\mathbf{q}$ [m/d] is the specific discharge vector and h [m] is the hydraulic head. Note that (3) is written in terms of $\mathbf{q}$, therefore the spatial variability of the ϕ field does not play a role in the solution of the groundwater flow problem. After solving (3), groundwater velocity is obtained from $\mathbf{v}(\mathbf{x}) = -K(\mathbf{x})\nabla h(\mathbf{x})/\phi(\mathbf{x})$, and used as input to the contaminant transport model. The contaminant transport equation is then including the ϕ field variability for both conservative and reactive chemical species.

As previously mentioned, to improve our understanding of the joint $K - \phi$ heterogeneity on transport and its role in contaminated groundwater management, we simulate contaminant transport for non-reactive and reactive species. The latter case will be linked to a dose-response model to evaluate the adverse health effects associated with contaminant exposure.

Reactive transport A contaminant is released along a vertical 2D plane of areal extent A_s. Contaminant mass fluxes or concentrations are measured at multiple control planes (CPs) located at different longitudinal distances from the source zone. Fig. 2 illustrates a sketch of the problem under investigation. Following the work of Henri et al. (2015), the aquifer is contaminated by tetrachloroethylene (PCE), a DNAPL product often identified in groundwater (Fay and Mumtaz, 1996). We assume that PCE is entrapped in the source area and slowly dissolves in time, originating a long-term contamination that moves downgradient. In the presence of an anaerobic environment, PCE undergoes chemical degradation that generates trichloroethylene (TCE), a byproduct that in turn reacts and degrades into cis-Dichloroethylene (DCE). DCE degrates then into vinyl chloride (VC), which will finally produce ethene. The US Environmental Protection Agency (EPA) classifies PCE, TCE and DCE as probable human carcinogenic products, whereas categorizes VC as a human carcinogen (U.S. Environmental Protection Agency, 1997).

The reactive transport of PCE and its daughter products can be described by the following system of equations, where subscript i indicates

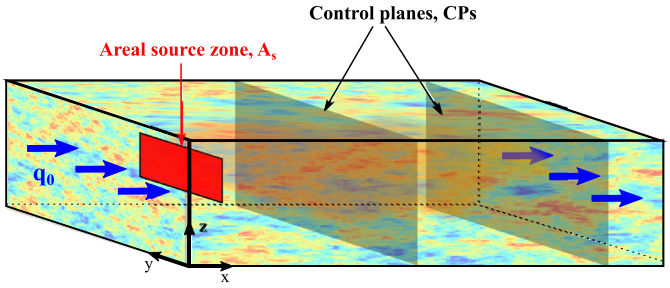

Fig. 2. Schematic illustration of the problem under investigation: the contaminant is released within the areal source zone, A_s. A uniform-in-the average natural base flow, q_0, takes place along the $x-$direction, contaminant mass fluxes or concentrations are measured at control planes (CPs).

a specific contaminant within the toxic PCE degradation chain (i.e., i=1: PCE; i=2: TCE; i=3: DCE and i=4: VC):

$$\phi R_i \frac{\partial C_i}{\partial t} - \nabla \cdot (\phi \mathbf{D} \nabla C_i) + \nabla \cdot (\mathbf{q} C_i) = y_i k_{i-1} \phi C_{i-1} - k_i \phi C_i + s(\mathbf{x}, t)\delta_{i1}, \quad \forall i = 1, \dots, 4, \tag{4}$$

where C_i [g/m^3] is the resident contaminant concentration of the ith species, $\mathbf{D}$ [m^2/d] represents the hydrodynamic dispersion tensor whose components along the x-, y- and z- direction are respectively $D_{xx} = \alpha_x v$, $D_{yy} = \alpha_y v$ and $D_{zz} = \alpha_z v$, with v [m/d] indicating groundwater velocity of the grid block. Here, α_x, α_y and α_z are respectively the longitudinal (along x), transverse horizontal (along y) and transverse vertical (along z) dispersivity coefficients, assumed to be constant for all the contaminant species. Furthermore, R_i represents the retardation factor, k_i [d^{-1}] indicates the first-order contaminant degradation rate and y_i [g g^{-1}] symbolizes the effective yield coefficient for any reactant or product pair. The latter represents the ratio between the generated mass of species i and the degraded mass of species $i-1$. We assume that biodegradation does not occur in the sorbed phase and that sorption reactions follow a linear sorption isotherm (see Henri et al., 2015, and references therein). δ_{i1} indicates the Kronecker delta function.

Note that in our study we account for the main characteristics of DNAPL mass discharge by linking the DNAPL source strength to the DNAPL mass remaining in the source zone (Falta et al., 2005). The source zone is then conceptualized as a control plane from which the temporal evolution of the contaminant fluxes is simulated using integrative parameters in line with the architecture of the DNAPL. We consider a time-dependent dissolution rate $s(\mathbf{x}, t)$ of PCE leaving the areal source, A_s, starting from no contamination at initial time $t = 0$. Following the approach described in Henri et al. (2015), we employ the mass-depletion model proposed in the literature (Parker and Park, 2004; Rao et al., 2001):

$$\frac{c_s(t)}{c_0} = \left(\frac{m(t)}{m_0}\right)^{\Gamma}, \tag{5}$$

where c_s is the flux-averaged concentration of the dissolved DNAPL species, i.e., PCE, leaving A_s, c_0 is the initial contaminant concentration at the source zone, m is the mass of DNAPL remaining in the source zone and Γ represents the mass-depletion constant accounting for changes of the interfacial surface area while the mass at the source diminishes. The flux concentration of PCE leaving the areal source is then expressed as in Parker and Park (2004):

$$c_s(t) = \frac{c_0}{m_0^{\Gamma}} \left\{ -\frac{Q_s c_0}{\lambda_s m_0^{\Gamma}} + \left({m_0}^{1-\Gamma} + \frac{Q_s c_0}{\lambda_s m_0^{\Gamma}} \right) e^{(\Gamma-1)\lambda_s t} \right\}^{\frac{\Gamma}{1-\Gamma}}, \tag{6}$$

where m_0 is the initial contaminant mass at the source, Q_s represents the groundwater volumetric discharge rate through the source zone while λ_s is the first-order degradation constant of PCE at the source (Henri et al., 2015). The function $s(x, t)$, i.e., the time-dependent dissolution rate at the source, is given by:

$$s(\mathbf{x}, t) = q_s c_s(t) \delta(x - x_{inj}) \Omega(\mathbf{x} \in A_s), \tag{7}$$

where $q_s = Q_s / A_s$, and $\Omega(\mathbf{x} \in A_s)$ is an indicator function equal to one if $x \in A_s$ and equal to zero elsewhere.

In Section 2.3, we present the dose-response model employed to compute the adverse health risk caused by the reactive chemicals degradation chain (i.e., PCE → TCE → DCE → VC).

Non-reactive transport With the goal of isolating the influence of heterogeneity in the aquifer geological properties K and ϕ on transport from the chemical reactions component, we also simulate transport of a non-reactive tracer. In this case, similarly to the reactive transport simulations, groundwater flow is also governed by Eqs. (2) and (3), whereas contaminant transport through the porous media is expressed by (4) with chemical reactions set to zero. During the conservative contaminant transport simulations the tracer is instantaneously and homogeneously released within A_s and we investigate the first arrival times and peak mass fluxes through the control planes and corresponding uncertainties.

2.3. Health risk model

Being the human health risk the EPM of concern for the reactive transport case, we follow the work of Maxwell and Kastenberg (1999), Henri et al. (2015), and Zarlenga et al. (2016) and adopt a Poisson model (U.S. Environmental Protection Agency, 1989) to evaluate the human incremental lifetime cancer risk (ILCR), $R_i(x)$ associated to an exposure to the contaminant i at the CP location x:

$$R_i(x) = 1 - \exp[-ADD_i(x) \times CPF_i], \tag{8}$$

where CPF_i [kg d/mg] indicates the metabolized cancer potency factor related to contaminant i and ADD_i [mg/(kg d)] is the average daily dose. In this work, risk is due to human exposure by direct ingestion and:

$$ADD_i(x) = \bar{c}_i(x) \frac{IR}{BW} \frac{ED \times EF}{AT}. \tag{9}$$

In Eq. (9), IR is the water ingestion rate [L/d], BW is the body weight [kg], ED symbolizes the exposure duration [y], EF is the daily exposure frequency [d/y] and AT indicates the expected lifetime [d].

In our study, $\bar{c}_i(x)$ [g/m^3] in (9) represents the flux-averaged concentration (Kreft and Zuber, 1979) at a CP situated at a given longitudinal distance x. This variable is identified both as: (a) the peak flux-averaged concentration and (b) the maximum exposure duration (ED) averaged (flux-averaged) concentration. The manner in which $\bar{c}_i(x)$ is evaluated can lead to different groundwater management strategies (de Barros and Rubin, 2008). It is therefore important to evaluate both cases (a) and (b) above, the first case being the worst scenario that can provide a conservative risk estimate. In the second case (b) $\bar{c}_i(x)$ is equal to the maximum running averaged concentration, over the ED interval, of the contaminant concentration BTC at the CP (Henri et al., 2015; Maxwell and Kastenberg, 1999) and is mathematically given by:

$$\bar{c}_i(x) = \max_{t>0} \left\{ \frac{1}{ED} \int_t^{t+ED} c_i(\tau; x) d\tau \right\}, \tag{10}$$

where $c_i(\tau; x)$ is the flux-averaged concentration observed at the CP location.

Given that we consider the degradation of PCE into sub-products, parent and daughter species are likely to be present simultaneously in the aquifer. The total risk of the chemical mixture (denoted by R_T), in the presence of low concentrations (less than 300 ppm), can then be identified as the summation of the individual risks caused by each chemical product (Feron et al., 1981) as follows:

$$R_T(x) = \sum_{i=1}^{4} R_i(x). \tag{11}$$

The health risk model parameters employed to compute the total ILCR, i.e., R_T (11), at the CPs, are listed in Table 1.

Table 1
Risk model parameters used in the numerical simulations.

Parameter	Symbol	Value			
Ingestion rate	IR	1.4 l/d			
Body weight	BW	70 kg			
Exposure duration	ED	30 y			
Exposure frequency	EF	350 d/y			
Average time of expected lifetime	AT	25550 d			
		PCE	TCE	DCE	VC
Cancer potency factor	CPF_i	0.0021	0.011	0.6	1.5

3. Methodology

General set-up In order to analyze contaminant transport and corresponding uncertainties throughout the 3D aquifer we employ a stochastic Monte Carlo (MC) framework that accounts for uncertain K and ϕ distributions. Five hundred equally likely K and ϕ fields are generated and, for each field, the groundwater flow and contaminant transport equations are numerically solved. Results are then statistically analyzed over the ensemble of MC realizations.

The 3D computational domain is characterized by dimensions $L_x \times L_y \times L_z = 700\text{ m} \times 400\text{ m} \times 100\text{ m}$ and discretized into $350 \times 200 \times 100$ cells (i.e., cells dimensions of $\Delta_x = \Delta_y = 2$ m and $\Delta_z = 1$ m). A large number of particles (10^4) is uniformly injected within the source area $A_s = L_{sy} \times L_{sz} = 70\text{ m} \times 20\text{ m}$, located at $x = x_{inj} = 50$ m and transversely centered within the aquifer domain. Note that the choice of the number of particles used in our simulations is based on a convergence analysis (not shown). In order to compute the BTCs, we employ a Kernel density estimator method that allows the automatization of the BTCs' reconstruction process and provides a better quality of results for the same number of injected particles (Fernàndez-Garcia and Sanchez-Vila, 2011). A set of 7 CPs are positioned at different distances along the x- direction (henceforth denoted by x_{CP}): 85 m, 100 m, 120 m, 200 m, 300 m, 400 m and 600 m.

The log-conductivity field $Y \equiv \ln[K]$ is spatially heterogeneous and represented by a Multi-Gaussian RSF, characterized by a Gaussian covariance function of ranges λ_x, λ_y and λ_z respectively along the x-, y- and z-direction, mean $\langle Y \rangle$ and variance σ_Y^2. For the computational analysis, we set $\lambda_x = \lambda_y = 35$ m and $\lambda_z = 10$ m. A sequential multi-Gaussian simulator (Remy et al., 2009) is employed to produce the ensemble of Y field realizations.

Based on the data reported in Section 2.1, we assume that the heterogeneous K field is positively correlated to the heterogeneous ϕ field and that the relationship between the two geological attributes can be described through the KC relationship (1). From each heterogeneous K field realization, we then obtain the corresponding spatially variable ϕ field, by applying the KC Eq. (1). To do so we invert the KC relationship by means of the Matlab solver. Note that all the parameters of the KC relationship (1) are constant (see Table 2) and that the representative diameter of grains (d_e), in our case corresponding to d_{10}, is chosen within the range 0.1–3 mm given the suitability to obtain a good prediction of the permeability of sand from porosity data when d_{10} is within this range (Barahona-Palomo et al., 2011). We also point out that the possible $K - \phi$ field combinations considered in our analysis are unconditional since we are not referring to a specific site. We analyze the influence of heterogeneity on transport in the presence of (a) constant ϕ and heterogeneous K and (b) spatially variable ϕ positively correlated to heterogeneous K. The outputs of scenarios (a) and (b) can be compared since the constant value of ϕ in case (a) coincides with the average value of the heterogeneous ϕ field realizations (i.e., $\langle \phi \rangle$). The average porosity, $\langle \phi \rangle$, is roughly constant for all the MC realizations and can, therefore, be obtained by applying the geometric mean of K (indicated as K_G) in the KC equation above (1). This leads to a mean ϕ value of 0.23. In order to give a better idea of the range of ϕ values of our simulations, we present in Fig. 3 the histogram of ϕ for one random realization of the K field. The latter is characterized by $\sigma_Y^2 = 1$ and the mean value of ϕ obtained is 0.239 (i.e., 23.9%).

Table 2
Parameter set used for the numerical flow and transport simulations.

Parameter	Symbol	Value
Aquifer domain	(L_x, L_y, L_z)	(700 m, 400 m, 100 m)
Grid discretization	$(\Delta_x, \Delta_y, \Delta_z)$	(2 m, 2 m, 1 m)
Y ranges	$(\lambda_x, \lambda_y, \lambda_z)$	(35 m, 35 m, 10 m)
Variance of Y	σ_Y^2	1, 3
Average porosity	$\langle \phi \rangle$	0.23
Average hydraulic head gradient	J	0.07
Geometric mean of K	K_G	4.48 m/d
Water density	ρ	1000 kg/m^3
Gravity acceleration	g	9.81 m/s^2
Dynamic viscosity	μ	8.84×10^{-4} Pa × s
Mean particles diameter	d_e	2×10^{-4} m
Source area dimensions	L_{sy} x L_{sz}	70 m × 20 m
Source area location along x	x_{inj}	50 m
Longitudinal dispersivity	α_x	0.2 m
Transversal horizontal dispersivity	α_y	0.02 m
Transversal vertical dispersivity	α_z	0.02 m
Control planes location along x	x_{CP}	85 m, 100 m, 120 m, 200 m, 300 m, 400 m, 600 m

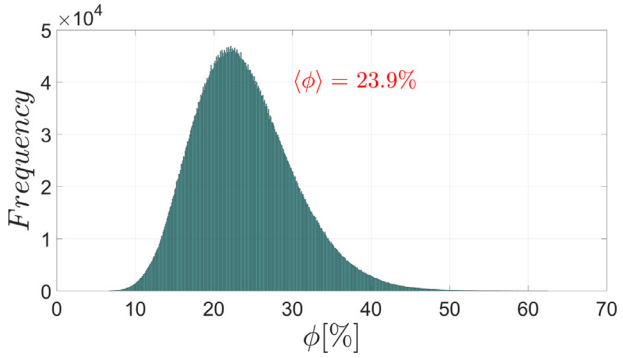

Fig. 3. Histogram of porosity values obtained by applying the KC Eq. (1) to one random realization of the conductivity field characterized by $\sigma_Y^2 = 1$. The average porosity is 23.9%.

Furthermore, different levels of heterogeneity of the Y field are explored: we consider both a mildly heterogeneous aquifer, represented by $\sigma_Y^2 = 1$ and a more heterogeneous system, characterized by $\sigma_Y^2 = 3$ for both the inert tracer and the reactive transport simulations. In each case, the variance of the $\ln(\phi)$ field, i.e., $\sigma^2_{\ln(\phi)}$, is one order of magnitude less that σ_Y^2, which is in agreement with the work of Hassan et al. (1998).

Groundwater fluxes are computed by means of the widely tested numerical model (finite-difference) MODFLOW (Harbaugh, 2005). Conservative and multispecies reactive transport are simulated through the RW3D code (Fernàndez-Garcia et al., 2005; Henri and Fernàndez-Garcia, 2014) using the random walk particle tracking method. The RW3D method uses the velocity field to advectically move particles and disturbs the motion by adding a random displacement to simulate dispersion. In order to obtain a continuous velocity field that fulfills the local solute mass balance, a hybrid scheme based on bilinear interpolation to handle the dispersion terms and on linear interpolation for the advective term is applied to the RWPT method. LaBolle et al. (1996) showed that this scheme can solve solute transport quite accurately within heterogeneous systems (Salamon et al., 2006). Given that we are employing heterogenous ϕ fields, the transport is also controlled by the spatially variable ϕ distribution (see Eq. (4)) and the values of the longitudinal, transverse horizontal, transverse vertical dispersivities, which are appropriately selected to account for sub-grid heterogeneity. The main input parameters used in the numerical solution of the flow and transport models are reported in Table 2.

Table 3
Reaction parameters.

Parameter	Symbol	Value			
		PCE	TCE	DCE	VC
First-order decay	k_i	0.005 d^{-1}	0.004 d^{-1}	0.003 d^{-1}	0.001 d^{-1}
Yield coefficient	y_i		0.79 g g^{-1}	0.74 g g^{-1}	0.64 g g^{-1}
Retardation factor	R_i	7.1	2.9	2.8	1.4

Reactive transport As far as the chemical parameters chosen for the reactive transport simulations, we employ constant values of biodegradation rates, which we select accordingly to the range of observed values listed by the US EPA (U.S. Environmental Protection Agency, 1999). Additionally, the choice of the retardation factors is based on the expected differences in mobility between the chlorinated solvents species (Henri et al., 2015; Lu et al., 2011). As explained in Henri and Fernàndez-Garcia (2014) the particle tracking algorithm represents the distribution of mass of each species by a different cloud of particles. The challenge is to define, from initial conditions, the species and position that a given particle will be associated with after a given time. To do so, each particle is defined by its position and species state at a given time and we aim to define the condition of the particle at a later time. The change in chemical state is determined from the species state transition probability matrix, whereas the corresponding particle motion is given by the first and second spatial moments. The motion of particles follows a standard random walk with time-dependent effective retardation and dispersion parameters that depend on the initial and final chemical state of the particle. Basically, the approach is based on the development of transition probabilities that describe the likelihood that particles belonging to a given species and location at a given time will be transformed into and moved to another species and location later on and these probabilities are derived from the solution matrix of the spatial moments governing equations (Henri and Fernàndez-Garcia, 2014). Table 3 shows the chemical reaction parameters adopted in our study.

During the reactive transport simulations particles are instantaneously and uniformly released within A_s. The first arrival time of the particles at the CPs is recorded and cumulative concentration BTCs are computed to obtain $c_i^h(t; x)$. The flux-averaged concentration of any reacting species i, $c_i(t; x)$, caused by the time-dependent injection described in (7), is computed through the principle of superposition as follows:

$$c_i(t;x) = \int_0^t c_s(\tau) c_i^{\delta}(t-\tau;x) d\tau, \tag{12}$$

where $c_i^{\delta}(\tau; x)$ represents the Dirac-input solution (i.e., instantaneous injection), of the concentration associated with the ith species. For numerical purposes, the source concentration $c_s(t)$ can be discretized in step functions according to:

$$c_s(t) = c_{s,0} H(t) + \sum_{j=1} \Delta c_{s,j} H(t - t_j), \tag{13}$$

with $H(t)$ indicating the Heaviside step function and $\Delta c_{s,j} = c_{s,j} - c_{s,j-1}$. Eq. (12) is then given by:

$$c_i(t;x) = c_{s,0} c_i^h(t;x) + \sum_{j=1}^{t_j<t} \Delta c_{s,j} c_i^h(t - t_j; x). \tag{14}$$

In (14), $c_i^h(t; x)$ indicates the cumulative BTC of the ith species computed from an unitary mass source (Henri et al., 2015). Table 4 presents the mass transfer parameters adopted in the reactive case study.

The contaminant concentration BTCs, recorded from the MC ensemble at the observation CPs, are then employed to compute $\bar{c}_i(x)$ in the two ways previously illustrated (see Section 2.3) and to compute the associated increased lifetime cancer risk.

Table 4
Mass transfer parameters of the source zone selected for the reactive transport simulations.

Parameter	Symbol	Value
Mass depletion constant	Γ	0.1
Initial contaminant mass	m_0	900 kg
Initial contaminant concentration	C_0	0.02 g/m^3
Source first-order degradation constant	λ_s	5×10^{-5} d^{-1}

Non-reactive transport In the conservative tracer simulations we instantaneously inject 1 gr of contaminant mass uniformly within A_s and observe the contaminant mass flux, indicated as $\dot{m}$ [g/d] at the CPs, from which the EPMs under investigation are computed. We recall that contaminant concentrations can then be obtained by the ratio between the contaminant mass flux (measured at the control plane) and the volumetric water flux through the CP.

The results of the conservative and reactive transport MC simulations are post-processed to evaluate the impact of ϕ heterogeneity on risk statistics and illustrated in Section 4.

4. Results

4.1. Analysis for non-reactive contaminants

In this Section we show the effect of $K - \phi$ heterogeneity on the transport of an inert tracer over the ensemble of MC realizations. We first present the Cumulative Distribution Function (CDF) of early arrival times of contaminants and of peak contaminant mass fluxes at the CPs. We then quantify the relative difference between first and late arrival times of the tracer at the observation locations. We finally show the impact of aquifer connectivity on peak contaminant mass fluxes.

In order to understand the importance of realistically accounting for heterogeneous ϕ, we consider different scenarios: heterogeneous ϕ fields correlated to spatially variable K characterized by $\sigma_Y^2 = 1$ and $\sigma_Y^2 = 3$, and corresponding spatially averaged homogeneous ϕ coupled with heterogeneous K with $\sigma_Y^2 = 1$ and $\sigma_Y^2 = 3$.

4.1.1. CDF of first arrival times and peak mass fluxes

We present in Fig. 4 the CDF of dimensionless first arrival times, normalized by the mean advective time required to travel a distance of 1 range along the longitudinal direction, i.e., $t_{5\%}U/\lambda_x$, where U is the longitudinal mean velocity, given by $U = K_G J/\langle\phi\rangle$, with J being the hydraulic head gradient. For simplicity, we only show the CDFs at two CPs located, respectively, at $x = 200$ m, corresponding to dimensionless distance $\zeta = 4.29$ (in green) and $x = 600$ m, corresponding to $\zeta = 15.71$ (in red), with $\zeta = (x_{CP} - x_{inj})/\lambda_x$. Results at the other CPs are alike. Fig. 4(a) and (b) refers to $\sigma_Y^2 = 1$ and $\sigma_Y^2 = 3$, respectively. Dashed curves correspond to heterogeneous correlated $K - \phi$ fields and solid curves indicate simplified homogeneous ϕ and heterogeneous K.

Fig. 4 clearly illustrates that spatially variable ϕ has a strong impact on the conservative tracer first arrival time statistics. Accounting for ϕ heterogeneity increases the probability of detecting larger $t_{5\%}$ at the CPs, for both levels of heterogeneity of the Y field. In particular, the importance of including the spatial variability of ϕ increases as the CPs' distance from the contaminant injection source increases (compare

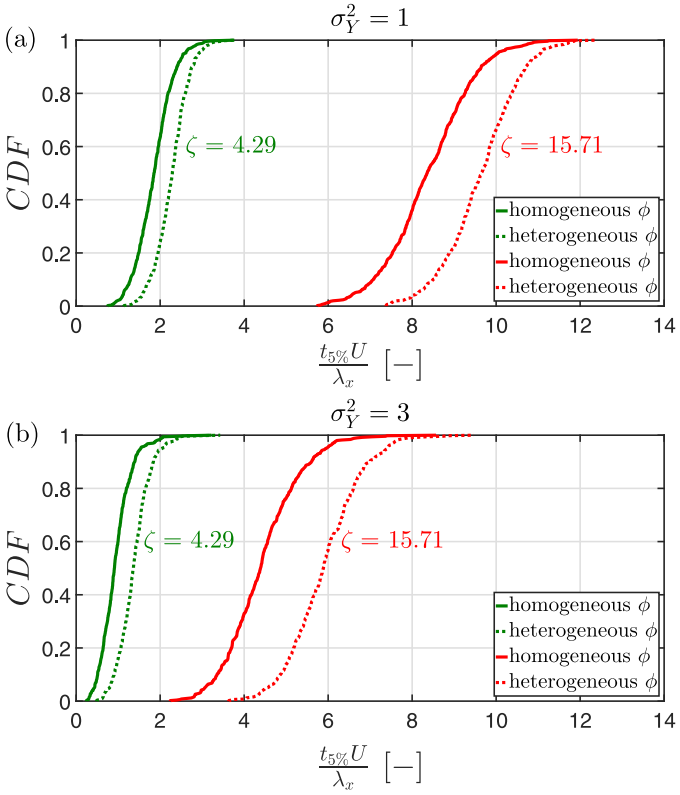

Fig. 4. Cumulative distribution function (CDF) of the first arrival times, $t_{5\%}$, of the contaminant mass at the CPs for $\sigma_Y^2 = 1$ (a) and $\sigma_Y^2 = 3$ (b). The CDF of dimensionless $t_{5\%}$ is indicated with dashed lines for heterogeneous ϕ fields and with solid lines for homogeneous ϕ fields. The green color indicates results at the CP located at dimensionless distance $\zeta = 4.29$ whereas the red color pictures results at the CP located at dimensionless distance $\zeta = 15.71$. (For interpretation of the references to colour in this figure legend, the reader is referred to the web version of this article.)

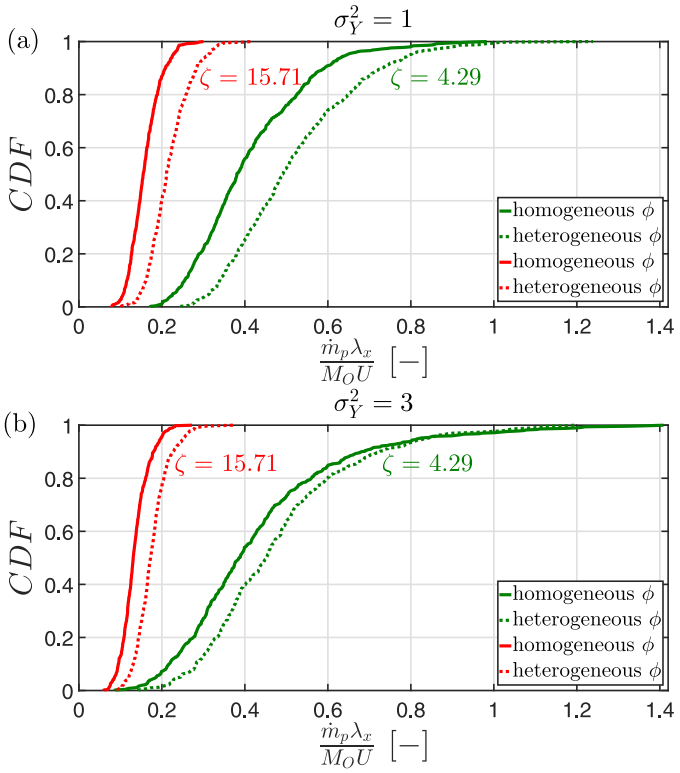

Fig. 5. Cumulative distribution function (CDF) of the contaminant mass peak, $\dot{m}_p$, at the CPs for $\sigma_Y^2 = 1$ (a) and $\sigma_Y^2 = 3$ (b). The CDF of $\dot{m}_p$ is indicated with dashed lines for heterogeneous ϕ fields and with solid lines for homogeneous ϕ fields. The green color indicates results at the CP located at dimensionless distance $\zeta = 4.29$ whereas the red color pictures results at the CP located at dimensionless distance $\zeta = 15.71$. (For interpretation of the references to colour in this figure legend, the reader is referred to the web version of this article.)

red curves versus green curves). Indeed, as the distance between the source and CP grows, the plume samples more heterogeneity of the system and the effect of considering variable ϕ strengthens. We also notice that increasing the heterogeneity of Y (see Fig. 4(b)) generally decreases $t_{5\%}$. Indeed larger σ_Y^2 increases the probability of occurrence of fast flow channels which leads to a decrease of first arrival times (compare Fig. 4(a) and (b)).

Subsequent Fig. 5 pictures the CDF of dimensionless peak mass fluxes ($\dot{m}_p$), normalized by the initial injected mass (M_0) over the time required to travel one range along x, indicated as $\dot{m}_p\lambda_x/(M_0U)$, at the two CPs located at dimensionless distances $\zeta = 4.29$ (in green) and $\zeta = 15.71$ (in red). Fig. 5(a) refers to $\sigma_Y^2 = 1$ whereas Fig. 5(b) to $\sigma_Y^2 = 3$. As before, dashed curves correspond to heterogeneous ϕ while solid curves indicate the outcome of considering homogeneous ϕ. Results at the remaining CPs show comparable outcomes.

From Fig. 5 we observe that the significance of accounting for coupled heterogeneous $K - \phi$ fields on transport predictions decreases when the EPM of interest is $\dot{m}_p$, as compared to $t_{5\%}$ (Fig. 4). This effect is more evident when the heterogeneity of the K-field is higher (compare Fig. 5(a) with (b)). We generally observe that the presence of heterogeneous ϕ fields increases the chance of observing higher peak mass fluxes as compared to homogeneous ϕ realizations for both observation locations and levels of heterogeneity of the Y field. In fact the positive correlation between the $K - \phi$ fields decreases the macrodispersion of the plume along the longitudinal direction, which produces higher peak mass fluxes at the observation locations. The decrease of plume dispersion is a result of a diminished variance of the groundwater velocity field in the presence of a positive correlation between ϕ and K. In fact lower velocity variance implies smaller velocity fluctuations which are the main factors driving dispersion. Lower plume dispersion along the longitudinal direction in the presence of positive $K - \phi$ correlation is in line with the findings of Hassan et al. (1998). Reduced longitudinal dispersion is also in agreement with the detection of later first arrival times when ϕ is modeled as heterogeneous and positively correlated to K (see dashed curves in Fig. 4) (Hassan et al., 1998). Moreover the effect of porosity variability on $\dot{m}_p$ increases for mildly heterogeneous aquifers (i.e., $\sigma_Y^2 = 1$), as compared to an aquifer with higher Y heterogeneity (i.e., $\sigma_Y^2 = 3$). This is also in agreement with the work of Hassan et al. (1998). We also notice lower peak mass fluxes at the CP located further away from A_s (i.e., at $\zeta = 15.71$, in red) according to the fact that plume dispersion increases as the plume travels longer and samples more aquifer heterogeneity. The results presented in Figs. 4 and 5 show the importance of incorporating the spatial variability in ϕ when predicting early arrival times and peak mass fluxes.

Since the heterogeneity of the ϕ field impacts the plume macrodispersion, we analyze the relative plume dispersion for the different scenarios investigated in the following Section 4.1.2.

4.1.2. Relative plume dispersion

The macro-scale dispersive behavior of the solute plume under uniform or spatially random ϕ fields, coupled with heterogeneous K realizations, is additionally explored in Fig. 6. In the latter, we present box plots of $\Delta\tau$, defined as:

$$\Delta\tau = \frac{t_{95\%} - t_{5\%}}{t_{95\%}}. \tag{15}$$

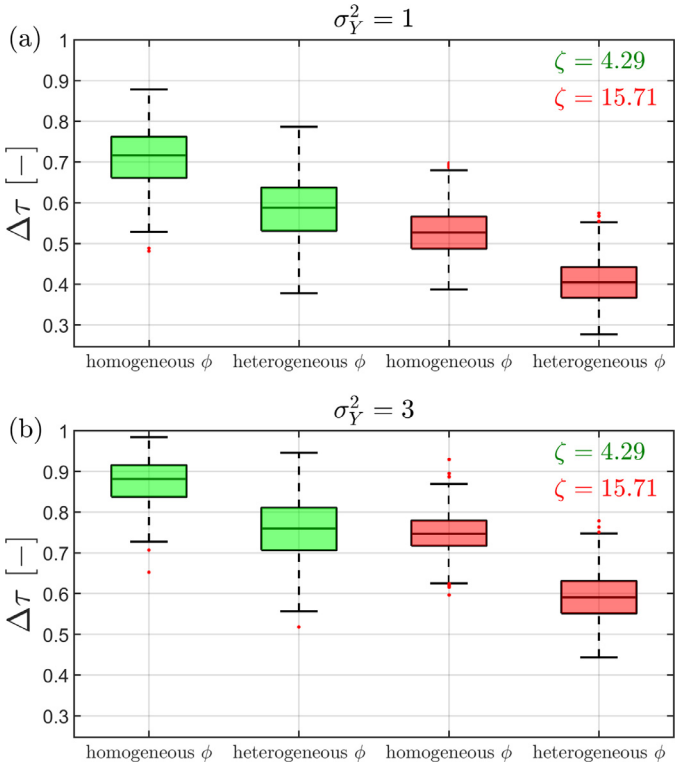

Fig. 6. Box plots of $\Delta\tau$ (15) for homogeneous and heterogeneous ϕ and for $\sigma_Y^2 = 1$ (a) and $\sigma_Y^2 = 3$ (b). The green and red colors respectively indicate the results at the CP located at dimensionless distance $\zeta = 4.29$ and $\zeta = 15.71$. (For interpretation of the references to colour in this figure legend, the reader is referred to the web version of this article.)

$t_{95\%}$ is identified as the time of arrival of 95% of the initial injected mass, M_0. $\Delta\tau$ can represent a measure of the relative plume dispersion since it quantifies the relative difference between the first (i.e., $t_{5\%}$) and late arrival times (i.e., $t_{95\%}$) of the tracer at the CPs. In Fig. 6 the green boxes indicate the results at the CP located at dimensionless distance $\zeta = 4.29$ whereas the red boxes refer to the outcomes at the CP situated at $\zeta = 15.71$, results at the additional CPs being similar. The thickness of the box plots equals the lag between the first and third quartiles of the probability distribution of $\Delta\tau$. Fig. 6(a) refers to $\sigma_Y^2 = 1$ whereas Fig. 6(b) to $\sigma_Y^2 = 3$.

When we compare the box plots of $\Delta\tau$ for homogeneous and heterogeneous ϕ, for both CPs locations and σ_Y^2 values, we observe that $\Delta\tau$ values are lower when ϕ is modeled as heterogeneous. This is because, as explained before, the longitudinal dispersion of the plume decreases when ϕ is positively correlated to K, leading to a smaller difference between first ($t_{5\%}$) and late ($t_{95\%}$) arrival times of the plume at the CPs. Accordingly, the range of $\Delta\tau$ presents higher values for all scenarios (homogeneous and heterogeneous ϕ and different CPs locations) when $\sigma_Y^2 = 3$, i.e., under higher heterogeneity of the Y field we observe a higher chance of fast flow channels (which decrease $t_{5\%}$) as well as increased longitudinal dispersion. Finally, in agreement with previous results, the difference between the range of $\Delta\tau$ values between the constant ϕ and heterogeneous ϕ cases increases for the CP located further away from the injection area (red box plots) for both levels of heterogeneity of Y. This confirms that the importance of modeling ϕ variability increases as the tracer travels longer through the heterogeneous aquifer domain.

4.1.3. Impact of connectivity on risk

Our analysis on the importance of accounting for ϕ spatial variability on the inert tracer transport statistics ends with analyzing the effect of aquifer connectivity on peak mass fluxes for the different scenarios considered. Previous results (see Figs. 4 and 6) showed how heterogeneity in ϕ and K affected solute arrival times. As a consequence, these heterogeneities can be expected to impact flow connectivity. We analyze here how $K - \phi$ variability affects connectivity and its predictive capabilities on the peak mass flux at a given CP. Connectivity can be described by different metrics (Knudby and Carrera, 2005; Rizzo and de Barros, 2017) and, in line with the work of Henri et al. (2015), we employ a dynamic connectivity metric, which depends on both groundwater flow and contaminant transport parameters (Knudby and Carrera, 2005). The selected connectivity metric, indicated as CI [-], is given by the ratio between the effective hydraulic conductivity, K_{eff}, and the geometric mean of K, K_G:

$$CI = \frac{K_{eff}}{K_G} \simeq \frac{1}{t_{50\%}} \frac{(x_{cp} - x_{inj})\langle\phi\rangle}{K_G J}, \tag{16}$$

with $t_{50\%}$ being the time of arrival of 50% of the initial injected mass at the CP of interest. The remaining parameters have been defined in Table 2. Note that the average ϕ value (i.e., $\langle\phi\rangle$) has been employed to compute CI for both the homogeneous and heterogeneous ϕ simulations. In this analysis, we identify the peak contaminant mass flux ($\dot{m}_p$) at the observation location (i.e., CP) as a measure of risk.

Fig. 7 shows scatter plots of dimensionless $\dot{m}_p$ versus CI (16). Every circle in Fig. 7 corresponds to a different MC realization and for simplicity only results at CPs located at dimensionless distance $\zeta = 1$ (in red) and $\zeta = 4.29$ (in green) are reported as the observations at the remaining CPs are similar. Full circles correspond to the outcome of considering homogeneous ϕ, whereas empty circles indicate the output of more realistic heterogeneous ϕ conditions. Fig. 7(a) refers to $\sigma_Y^2 = 1$ while Fig. 7(b) reports the results of $\sigma_Y^2 = 3$.

A linear regression between $\dot{m}_p$ and CI is identified for both homogeneous (full circles) and heterogeneous (empty circles) ϕ fields, CP location and σ_Y^2 value. Indeed, under higher CI values, corresponding to the presence of preferential flow channels, ergo lower $t_{50\%}$ (16), a higher chance of detecting higher $\dot{m}_p$ values at the CPs under investigation is identified. We observe that the slope of the linear regression line, whose equation is reported in gray for homogeneous ϕ and in black for heterogeneous ϕ, is higher when ϕ is heterogeneous and positively correlated to K as compared to simplified homogeneous ϕ for both CPs and for both levels of heterogeneity of Y. Therefore, under realistic heterogeneous ϕ conditions and under the assumption that the $K - \phi$ relationship can be described through the KC Eq. (1), an increased chance of observing higher $\dot{m}_p$, i.e. having higher risk, emerges as compared to constant ϕ conditions, for the same CI value. This could be attributed to the lower macro-scale spreading/dispersion of the contaminant plume under positive $K - \phi$ correlation, which results in higher $\dot{m}_p$ at the sensitive location. We also notice that a larger σ_Y^2 (Fig. 6(b)) favors the formation of preferential channels, hence higher CI values and corresponding $\dot{m}_p$ values (compare Fig. 7(a) and (b)). Results at the remaining CPs locations are similar and we generally observe a decrease of the coefficient of determination (R^2) of the regression line between CI and $\dot{m}_p$ values as the CP distance from A_s increases.

Our results suggest that realistic heterogeneous ϕ conditions are associated with higher values of $\dot{m}_p$, corresponding to higher health risk at sensitive locations, therefore considering simplified constant ϕ conditions could be misleading, i.e. lead to underestimated risks. We also foresee that the effects of incorporating porosity variability on transport observables could potentially be emphasized in the presence of non-Gaussian K fields which present higher probability of well-connected zones of high K values (Gómez-Hernández and Wen, 1998; Henri et al., 2015). For example, the work of Libera et al. (2017b) showed that higher solute peak concentrations are detected at extraction wells as the departure of the non-Gaussian Y fields from a Gaussian structure increases.

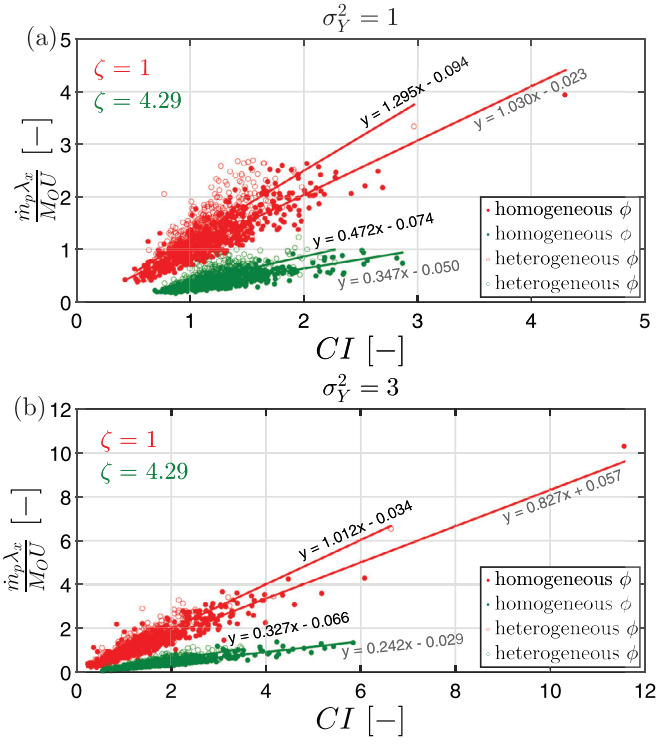

Fig. 7. Peak mass flux, $\dot{m}_p$, versus connectivity metric, CI (16), for $\sigma_Y^2 = 1$ (a) and $\sigma_Y^2 = 3$ (b). The red color indicates results at the CP located at dimensionless distance $\zeta = 1$ whereas the green color pictures results at the CP located at dimensionless distance $\zeta = 4.29$. Full circles indicate homogeneous ϕ and empty circles indicate heterogeneous ϕ. The regression line is plotted in gray for homogeneous ϕ and in black for heterogeneous ϕ for both CPs locations. The coefficient of determination (R^2) of the regression line for $\sigma_Y^2 = 1$ at the CP located at dimensionless distance $\zeta = 1$ are $R^2 = 0.778$ for homogeneous ϕ, $R^2 = 0.599$ for heterogeneous ϕ and $R^2 = 0.656$ for homogeneous ϕ, $R^2 = 0.444$ for heterogeneous ϕ at the CP located at dimensionless distance $\zeta = 4.29$. The coefficient of determination (R^2) of the regression line for $\sigma_Y^2 = 3$ at the CP located at dimensionless distance $\zeta = 1$ are $R^2 = 0.871$ for homogeneous ϕ, $R^2 = 0.816$ for heterogeneous ϕ and $R^2 = 0.845$ for homogeneous ϕ, $R^2 = 0.728$ for heterogeneous ϕ at the CP located at dimensionless distance $\zeta = 4.29$. (For interpretation of the references to colour in this figure legend, the reader is referred to the web version of this article.)

4.2. Analysis for reactive contaminants: Implications in increased lifetime cancer risk

Results in this Section refer to the reactive contaminant transport simulations, i.e. to the degradation chain of chlorinated solvents (PCE → TCE → DCE → VC). We analyze the statistics of the total increased lifetime cancer risk, $R_T(x)$ (11), for the scenarios under investigation. We first present the spatial distribution of the low-order moments, i.e. the ensemble mean and the coefficient of variation, of R_T, and we then show the complete statistical characterization of the PDF of R_T.

The outcomes of accounting for heterogeneous ϕ are represented with dashed lines while the results of constant ϕ are illustrated with solid lines in Figs. 8–10. The results of considering $\sigma_Y^2 = 1$ are pictured in magenta and the outcomes for $\sigma_Y^2 = 3$ are illustrated in blue.

4.2.1. Low order moments of $\mathbf{R_T(x)}$

Fig. 8 shows the spatial evolution of the mean value of R_T (11), denoted as $\langle R_T \rangle$, over the ensemble of MC simulations, when the peak concentration of the contaminant i at the CP (Fig. 8(a)) or the maximum running averaged concentration over the ED time (10) (Fig. 8(b)) is adopted to compute $R_T(x)$. $\langle R_T(x) \rangle$ quantifies the expected threat to the exposed community.

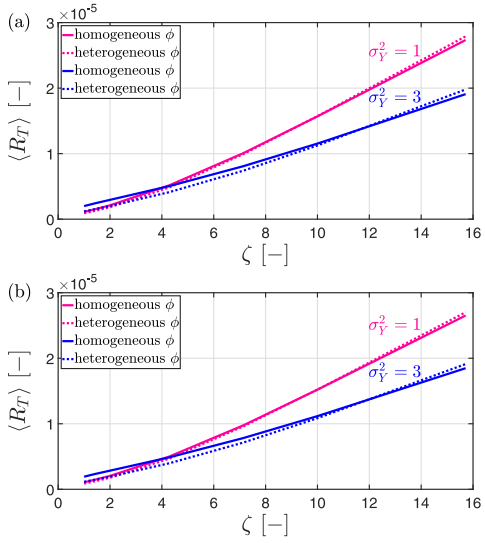

Fig. 8. Longitudinal spatial distribution of the mean total increased lifetime cancer risk, $\langle R_T \rangle$, when the maximum concentration (a) or the maximum running averaged concentration over the exposure duration (ED) time (b) are considered to compute R_T. The results for $\sigma_Y^2 = 1$ are represented in magenta and the results for $\sigma_Y^2 = 3$ are pictured in blue. Dashed curves correspond to heterogeneous ϕ fields and solid curves picture homogeneous ϕ. (For interpretation of the references to colour in this figure legend, the reader is referred to the web version of this article.)

We first notice that, for the current numerical set-up, the formula adopted to compute the flux-averaged contaminant concentration in Eq. (9) has only a very minor influence on the spatial evolution of $\langle R_T \rangle$ (compare Fig. 8(a) and (b)). We indeed notice that $\langle R_T \rangle$ is just slightly lower when we employ the maximum running averaged concentration to compute the risk (Fig. 8(b)), according to the fact that adopting the peak concentration represents the most conservative approach. We observe that $\langle R_T \rangle$ increases with CP distance since more toxic species are produced with time along the chemical degradation chain of PCE (Henri et al., 2015) in Fig. 8(a) and (b). In fact, cancer potency factors (CPF_i) increase during the degradation of PCE until VC is produced (see Table 1). In general, the influence of heterogeneity on the mean ILCR is almost unnoticeable in Fig. 8 (see dashed lines versus solid lines). The fact that accounting for ϕ heterogeneity has only a small impact on $\langle R_T(x) \rangle$ confirms that, also in the presence of reactive contaminants, the influence of incorporating ϕ variability depends on the metric of interest. Increasing the heterogeneity of the Y field (i.e., $\sigma_Y^2 = 3$, blue lines) decreases the magnitude of the mean ILCR along the longitudinal direction because of enhanced dispersion of the plume and subsequent dilution at CPs (Henri et al., 2015).

Fig. 9 shows the spatial evolution of the coefficient of variation of the total ILCR (i.e., $CV_{R_T}(x)$). We recall that $CV_{R_T}(x) = \sigma_{R_T}(x)/\langle R_T(x) \rangle$, with $\sigma_{R_T}(x)$ indicating the standard deviation of the total ILCR. Fig. 9(a) refers to the computation of $R_T(x)$ by considering the maximum contaminant concentration whereas Fig. 9(b) shows the same results when the maximum ED flux-averaged concentration (10) is adopted to compute $R_T(x)$. The coefficient of variation, $CV_{R_T}(x)$, measures the uncertainty associated with the risk estimate.

In agreement with what observed in Fig. 9, we also point out that the approach adopted to compute the flux-averaged concentration in Eq. (9) does not influence the risk uncertainty and the differences between Fig. 9(a) and (b) are imperceptible. We note that this remark is applicable to the current numerical set-up. We generally observe that the spatial evolution of CV_{R_T} presents an inverse correlation with $\langle R_T(x) \rangle$, in agreement with Henri et al. (2015). Therefore we identify lower mean total ILCR and more uncertain risk predictions close to the source while we observe higher mean risk and lower risk uncertainty further away for all

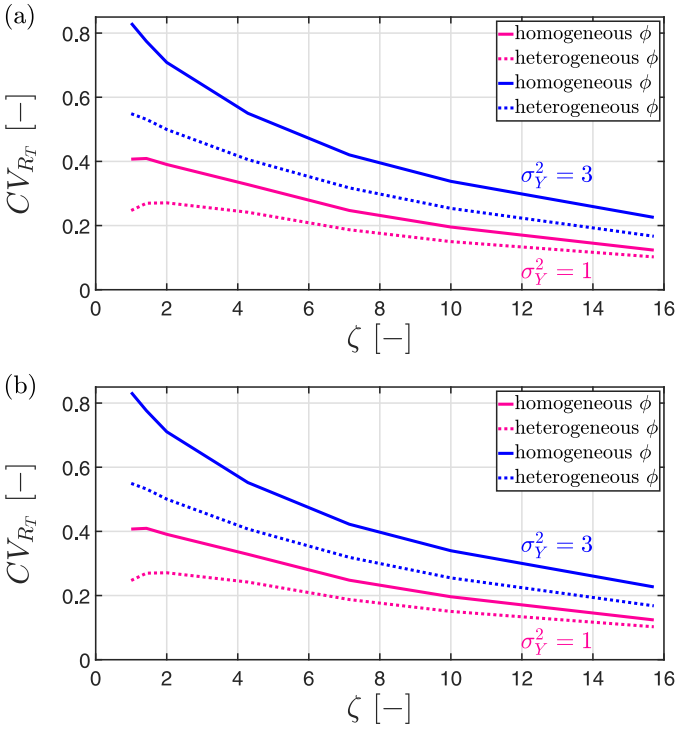

Fig. 9. Longitudinal spatial distribution of the coefficient of variation of the total increased lifetime cancer risk, CV_{R_T}, when the maximum concentration (a) or the maximum running averaged concentration over the exposure duration (*ED*) time (b) are considered to compute R_T. The results for $\sigma_Y^2 = 1$ are represented in magenta and the results for $\sigma_Y^2 = 3$ are pictured in blue. Dashed curves correspond to heterogeneous ϕ fields and solid curves picture homogeneous ϕ. (For interpretation of the references to colour in this figure legend, the reader is referred to the web version of this article.)

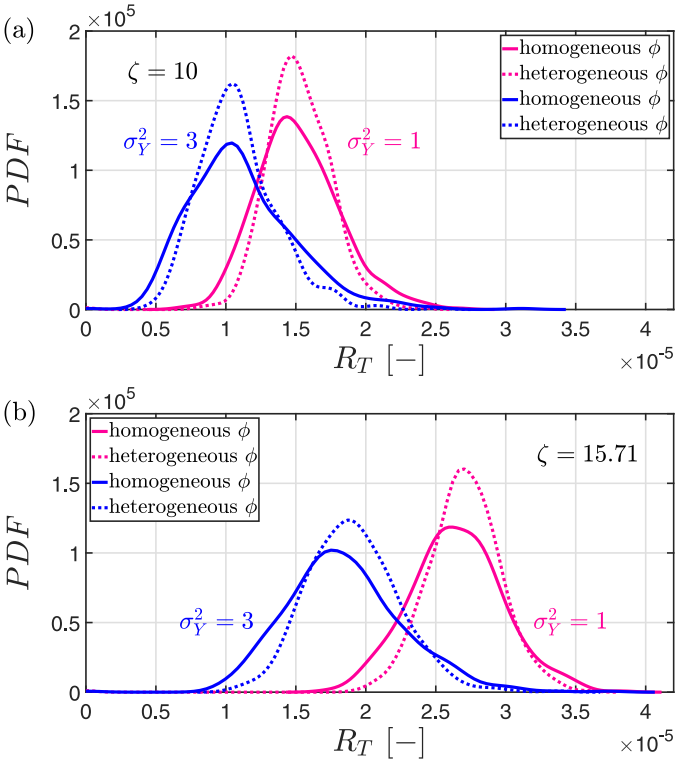

Fig. 10. Probability distribution function (PDF) of the total increased lifetime cancer risk, R_T, at the CP located at $\zeta = 10$ (a) and $\zeta = 15.71$ (b). The results for $\sigma_Y^2 = 1$ are represented in magenta and the results for $\sigma_Y^2 = 3$ are pictured in blue. Dashed curves correspond to heterogeneous ϕ fields and solid curves picture homogeneous ϕ. (For interpretation of the references to colour in this figure legend, the reader is referred to the web version of this article.)

the simulated scenarios. Larger risk uncertainty close to the source is expected since the plume is mainly controlled by advection at that stage (de Barros et al., 2009). Our results indicate that accounting for the heterogeneity in ϕ affects the risk uncertainty. Indeed, the positive correlation between ϕ and K leads to a reduction of the sample-to-sample fluctuation of the risk, and therefore to a reduction of $CV_{R_T}(x)$ for both levels of heterogeneity of the Y field (see dashed lines versus solid lines in both Fig. 9(a) and (b). This effect is emphasized when $\sigma_Y^2 = 3$.

The results presented in Figs. 8 and 9 show that the influence of ϕ heterogeneity is higher on risk uncertainty, i.e., $CV_{R_T}(x)$ (Fig. 9) than on the mean total ILCR, $\langle R_T(x) \rangle$, (Fig. 8). This can be justified by the fact that mean mass fluxes at large CPs are not significantly affected by local fluctuations of the flow field, as explained in Fiori et al. (2002). On the other hand, the first order analysis provided in Fiori et al. (2002) and Andričević and Cvetković (1998) shows that the variance of the mass flux over a control plane is sensitive to local heterogeneity.

4.2.2. *PDF of* R_T

We conclude the discussion on the influence of ϕ spatial heterogeneity on reactive transport by presenting the PDF of the ILCR in Fig. 10. The results in Fig. 10 refer to the computation of $R_T(x)$ by employing the maximum running averaged concentration over *ED* (10). Results at the CP located at $\zeta = 10$ are reported in Fig. 10(a), while the outcomes at $\zeta = 15.71$ are presented in Fig. 10(b).

The PDFs of R_T present a similar "Gaussian"-like shape under constant or random ϕ. These results are consistent with the findings of Henri et al. (2015, 2016). We observe that the impact of ϕ heterogeneity on the PDF of the ILCR, described below, is more pronounced when the CP is situated closer to the source for the case of $\sigma_Y^2 = 3$ (compare Fig. 10(a) with (b). In general accounting for ϕ heterogeneity (dashed PDFs) only slightly influences the mean value of R_T but significantly affects the uncertainty of R_T. We indeed notice that the R_T PDF is less spread when the heterogeneity of ϕ is modeled as compared to assuming constant ϕ (dashed PDFs versus solid PDFs). In particular the probability of observing values of R_T around $\langle R_T \rangle$ increases of more than 30% when the variability of ϕ is included in models' predictions for all scenarios considered except for the case of $\sigma_Y^2 = 3$ at the CP located at $\zeta = 15.71$, where this probability is around 20% higher under heterogeneous ϕ. Moreover, the full risk PDFs show the probability of observing extreme values of R_T. We observe that modeling the ϕ heterogeneity has influence on both the highest and lowest values of R_T and the probability of detecting extreme values of R_T decreases in the presence of spatially variable ϕ.

5. Conclusions

In this study we analyze the impact of the coupled spatial variability of ϕ and K on contaminant transport and probabilistic risk analysis. We employ a Monte Carlo framework to statistically analyze key EPMs, detected at observation locations. We analyze the impact of ϕ heterogeneity on contaminant arrival times and peak mass fluxes of tracers at control planes as well as on risk and on connectivity. We then show the implications of accounting for ϕ variability in probabilistic human health cancer risk analysis by considering human exposure to chlorinated solvents through the ingestion pathway. Our work leads to the following main key conclusions:

- The positive correlation between ϕ and K leads to a decrease of the plume macrodispersion with consequent higher peak mass fluxes, later first arrival times and earlier late arrivals at control planes. Higher peak mass fluxes correspond to higher health risk therefore including the spatial variability of ϕ in models' predictions is

essential for risk assessment associated with aquifer contamination and remediation. Moreover, a more accurate quantification of early and late arrival times is fundamental to respectively detect the potential hazard of a contaminant and to control the end-point of remediation (see e.g., Andričević and Cvetković, 1996; de Barros and Rubin, 2008).

- The relevance of incorporating the spatial variability of the ϕ field can depend on the metric of interest, for example our study shows that this relevance is emphasized when investigating contaminants' arrival times over peak mass fluxes at the observation control planes. This has important implications both to set-up modeling studies and in decision making processes (e.g., in risk assessment or aquifer remediation activities) in the context of a better allocation of resources. Indeed, available resources need to be prioritized and assigned in a defensible manner to ensure that unacceptable identified risks are reduced to acceptable levels.

- Modeling the ϕ field spatial variability as positively correlated to the heterogeneous K field significantly reduces the cancer risk uncertainty but only minorly influences the mean value of the total cancer risk at control planes. Our findings constitute then an important contribution for cancer risk uncertainty quantification however, adoptng more simplified and conservative models which assume homogeneous porosity does not highly impact the mean value of the total cancer risk.

We finally noticed that the effect of considering ϕ heterogeneity can be affected by the level of heterogeneity of the K field and by the source-to-CP distance. We recall that the results of our work are limited to positive correlation between ϕ and K expressed through the KC Eq. (1). Other empirical models can be adopted to compute the $K - \phi$ relationship and could potentially lead to different conclusions. Furthermore, other factors such as pumping operations (Libera et al., 2017a) and solute mass release rates at the source zone (de Barros, 2018) can impact the relative importance of hydrogeological heterogeneity. On a final note, we emphasize that our work represents a first step towards a more comprehensive global sensitivity analysis (GSA) that could lead to more general conclusions. Using polynomial chaos expansion (PCE) within a GSA can reduce the computational burden associated with Monte Carlo simulations. Utilizing PCE to perform GSA would allow to better understand the relevance of heterogeneous porosity with respect to heterogeneous hydraulic conductivity. Under the context of risk, PCE-based GSA was employed by different authors (e.g., Ciriello et al., 2013a; 2013b; Oladyshkin et al., 2012). Ciriello et al. (2013a) employed GSA to identify the influence of uncertain hydrogeological parameters on the first two statistical moments of the peak concentration. Ciriello et al. (2013b) applied a GSA through PCE to three transport models to identify the relative importance of model-dependent parameters, the space-time locations where the models are more sensitive to these parameters and to assist with parameters estimation. Oladyshkin et al. (2012) illustrated their GSA approach, based on arbitrary polynomial chaos expansion (aPC), on a 3D groundwater quality and health risk problem in a heterogeneous aquifer. Incorporating a GSA through PCE into the problem investigated in this work is topic of future research with the goal of reducing the computational burden normally associated with Monte Carlo simulations and to investigate the impact of considering different soil types on risk (e.g., Moore and Doherty, 2005).

Acknowledgments

Arianna Libera and Felipe P. J. de Barros acknowledge the support from the National Science Foundation under Grant No. 1654009. The authors acknowledge the constructive comments raised by three anonymous reviewers.

References

Aimrun, W., Amin, M., Eltaib, S., 2004. Effective porosity of paddy soils as an estimation of its saturated hydraulic conductivity. Geoderma 121 (3–4), 197–203.
Andričević, R., Cvetković, V., 1996. Evaluation of risk from contaminants migrating by groundwater. Water Resour. Res. 32 (3), 611–621.
Andričević, R., Cvetković, V., 1998. Relative dispersion for solute flux in aquifers. J. Fluid Mech. 361, 145–174.
Archie, G.E., 1950. Introduction to petrophysics of reservoir rocks. Am. Assoc. Pet. Geol. Bull. 34 (5), 943–961.
Atkins, J.E., McBride, E.F., 1992. Porosity and packing of holocene river, dune, and beach sands (1). Am. Assoc. Pet. Geol. Bull. 76 (3), 339–355.
Atkinson, C.D., McGowen, J.H., Bloch, S., Lundell, L.L., Trumbly, P.N., 1990. Braidplain and deltaic reservoir, Prudhoe Bay field, Alaska. In: Sandstone Petroleum Reservoirs. J.H. Barwis, J.G. McPherson, and J.R.J. Studlick, eds, Springer-Verlag, pp. 205–224.
Barahona-Palomo, M., Riva, M., Sanchez-Vila, X., Vazquez-Sune, E., Guadagnini, A., 2011. Quantitative comparison of impeller-flowmeter and particle-size-distribution techniques for the characterization of hydraulic conductivity variability. Hydrogeol. J. 19 (3), 603–612.
Barr, D.W., 2005. Discussion of æGoodbye, Hazen; Hello, Kozeny-Carman,g by W. David Carrier III. J. Geotech. Geoenviron. Eng. 131 (8), 1057–1058.
de Barros, F.P.J., 2018. Evaluating the combined effects of source zone mass release rates and aquifer heterogeneity on solute discharge uncertainty. Adv. Water Resour. 117, 140–150.
de Barros, F.P.J., Ezzedine, S., Rubin, Y., 2012. Impact of hydrogeological data on measures of uncertainty, site characterization and environmental performance metrics. Adv. Water Resour. 36, 51–63.
de Barros, F.P.J., Rubin, Y., 2008. A risk-driven approach for subsurface site characterization. Water Resour. Res. 44 (1).
de Barros, F.P.J., Rubin, Y., Maxwell, R.M., 2009. The concept of comparative information yield curves and its application to risk-based site characterization. Water Resour. Res. 45 (6).
Bear, J., 1979. Hydraulics of Groundwater. Mcgraw-Hill International Book Co., New York.
Bianchi, M., Zheng, C., 2016. A lithofacies approach for modeling non-Fickian solute transport in a heterogeneous alluvial aquifer. Water Resour. Res. 52 (1), 552–565.
Carman, P.C., 1937. Fluid flow through granular beds. Trans. Inst. Chem. Eng. 15, 150–166.
Carman, P.C., 1956. Flow of Gases through Porous Media.
Carrier III, W.D., 2003. Goodbye, Hazen; Hello, Kozeny-Carman. J. Geotech. Geoenviron. Eng. 129 (11), 1054–1056.
Ciriello, V., Di Federico, V., Riva, M., Cadini, F., De Sanctis, J., Zio, E., Guadagnini, A., 2013. Polynomial chaos expansion for global sensitivity analysis applied to a model of radionuclide migration in a randomly heterogeneous aquifer. Stochast. Environ. Res. Risk Assess. 27 (4), 945–954.
Ciriello, V., Guadagnini, A., Di Federico, V., Edery, Y., Berkowitz, B., 2013. Comparative analysis of formulations for conservative transport in porous media through sensitivity-based parameter calibration. Water Resour. Res. 49 (9), 5206–5220.
Dagan, G., 1986. Statistical theory of groundwater flow and transport: pore to laboratory, laboratory to formation, and formation to regional scale. Water Resour. Res. 22 (9S).
Doyen, P.M., 1988. Permeability, conductivity, and pore geometry of sandstone. J. Geophys. Res. 93 (B7), 7729–7740.
Fallico, C., 2014. Reconsideration at field scale of the relationship between hydraulic conductivity and porosity: the case of a sandy aquifer in south italy. Scientif. World J. 2014.
Falta, R.W., Rao, P.S., Basu, N., 2005. Assessing the impacts of partial mass depletion in dnapl source zones: i. analytical modeling of source strength functions and plume response. J. Contam. Hydrol. 78 (4), 259–280.
Fay, R., Mumtaz, M., 1996. Development of a priority list of chemical mixtures occurring at 1188 hazardous waste sites, using the hazdat database. Food Chem. Toxicol. 34 (11–12), 1163–1165.
Fernàndez-Garcia, D., Illangasekare, T.H., Rajaram, H., 2005. Differences in the scale-dependence of dispersivity estimated from temporal and spatial moments in chemically and physically heterogeneous porous media. Adv. Water Resour. 28 (7), 745–759.
Fernàndez-Garcia, D., Sanchez-Vila, X., 2011. Optimal reconstruction of concentrations, gradients and reaction rates from particle distributions. J. Contam. Hydrol. 120, 99–114.
Feron, V., Hendriksen, C., Speek, A., Til, H., Spit, B., 1981. Lifespan oral toxicity study of vinyl chloride in rats. Food Cosmet. Toxicol. 19, 317–333.
Fiori, A., 2001. The lagrangian concentration approach for determining dilution in aquifer transport: theoretical analysis and comparison with field experiments. Water Resour. Res. 37 (12), 3105–3114.
Fiori, A., Berglund, S., Cvetkovic, V., Dagan, G., 2002. A first-order analysis of solute flux statistics in aquifers: the combined effect of pore-scale dispersion, sampling, and linear sorption kinetics. Water Resour. Res. 38 (8).
Franzmeier, D., 1991. Estimation of hydraulic conductivity from effective porosity data for some indiana soils. Soil Sci. Soc. Am. J. 55 (6), 1801–1803.
Freeze, R. A., Cherry, J. A., 1979. Groundwater, 604pp.
Gelhar, L.W., 1986. Stochastic subsurface hydrology from theory to applications. Water Resour. Res. 22 (9S).
Gómez-Hernández, J.J., Wen, X.-H., 1998. To be or not to be multi-Gaussian? a reflection on stochastic hydrogeology. Adv. Water Resour. 21 (1), 47–61.
Grau, A., 2000. Material Balance: Quartz Cement vs. Internal Sources of Silica, East Brae Field, Offshore United Kingdom: Ph.D. Thesis, Colorado School of Mines, Golden Colorado.

Harbaugh, A.W., 2005. MODFLOW-2005, The US geological survey modular ground-water model: The ground-water flow process. US Department of the Interior, US Geological Survey Reston.
Hassan, A.E., 2001. Water flow and solute mass flux in heterogeneous porous formations with spatially random porosity. J. Hydrol. 242 (1), 1–25.
Hassan, A.E., Cushman, J.H., Delleur, J.W., 1998. Significance of porosity variability to transport in heterogeneous porous media. Water Resour. Res. 34 (9), 2249–2259.
Henri, C.V., Fernàndez-Garcia, D., 2014. Toward efficiency in heterogeneous multispecies reactive transport modeling: a particle-tracking solution for first-order network reactions. Water Resour. Res. 50 (9), 7206–7230.
Henri, C.V., Fernàndez-Garcia, D., de Barros, F.P.J., 2015. Probabilistic human health risk assessment of degradation-related chemical mixtures in heterogeneous aquifers: risk statistics, hot spots, and preferential channels. Water Resour. Res. 51 (6), 4086–4108.
Henri, C.V., Fernàndez-Garcia, D., De Barros, F.P., 2016. Assessing the joint impact of dnapl source-zone behavior and degradation products on the probabilistic characterization of human health risk. Adv. Water Resour. 88, 124–138.
Hu, B.X., Meerschaert, M.M., Barrash, W., Hyndman, D.W., He, C., Li, X., Guo, L., 2009. Examining the influence of heterogeneous porosity fields on conservative solute transport. J. Contam. Hydrol. 108 (3), 77–88.
Knudby, C., Carrera, J., 2005. On the relationship between indicators of geostatistical, flow and transport connectivity. Adv. Water Resour. 28 (4), 405–421.
Koltermann, C.E., Gorelick, S.M., 1995. Fractional packing model for hydraulic conductivity derived from sediment mixtures. Water Resour. Res. 31 (12), 3283–3297.
Kozeny, J., 1927. Über kapillare Leitung der Wasser in Boden. Royal Academy of Science, Vienna, Proc. Class I 136, 271–306.
Kreft, A., Zuber, A., 1979. On the use of the dispersion model of fluid flow. Int. J. Appl. Radiat. Isot. 30 (11), 705–708.
LaBolle, E.M., Fogg, G.E., Tompson, A.F., 1996. Random-walk simulation of transport in heterogeneous porous media: local mass-conservation problem and implementation methods. Water Resour. Res. 32 (3), 583–593.
Libera, A., de Barros, F.P.J., Guadagnini, A., 2017. Influence of pumping operational schedule on solute concentrations at a well in randomly heterogeneous aquifers. J. Hydrol. 546, 490–502.
Libera, A., de Barros, F.P.J., Riva, M., Guadagnini, A., 2017. Solute concentration at a well in non-Gaussian aquifers under constant and time-varying pumping schedule. J. Contam. Hydrol. 205, 37–46.
Lin, S., 1977. Longitudinal dispersion in porous media with variable porosity. J. Hydrol. 34 (1–2), 13–19.
Lu, C., Bjerg, P.L., Zhang, F., Broholm, M.M., 2011. Sorption of chlorinated solvents and degradation products on natural clayey tills. Chemosphere 83 (11), 1467–1474.
Luijendijk, E., Gleeson, T., 2015. How well can we predict permeability in sedimentary basins? deriving and evaluating porosity–permeability equations for noncemented sand and clay mixtures. Geofluids 15 (1–2), 67–83.
Maxwell, R., Kastenberg, W., 1999. Stochastic environmental risk analysis: an integrated methodology for predicting cancer risk from contaminated groundwater. Stochast. Environ. Res. Risk Assess. 13 (1), 27–47.
Moore, C., Doherty, J., 2005. Role of the calibration process in reducing model predictive error. Water Resour. Res. 41 (5).
Morin, R.H., 2006. Negative correlation between porosity and hydraulic conductivity in sand-and-gravel aquifers at cape cod, massachusetts, usa. J. Hydrol. 316 (1–4), 43–52.
Nelson, P.H., 2004. Permeability-porosity data sets for sandstones. Leading Edge 23 (11), 1143–1144.
Nelson, P.H., et al., 1994. Permeability-porosity relationships in sedimentary rocks. Log Analyst 35 (03).
Odong, J., 2007. Evaluation of empirical formulae for determination of hydraulic conductivity based on grain-size analysis. J. Am. Sci. 3 (3), 54–60.
Oladyshkin, S., de Barros, F., Nowak, W., 2012. Global sensitivity analysis: a flexible and efficient framework with an example from stochastic hydrogeology. Adv. Water Resour. 37, 10–22.
Panda, M.N., Lake, L.W., 1994. Estimation of single-phase permeability from parameters of particle-size distribution. Am. Assoc. Pet. Geol. Bull. 78 (7), 1028–1039.
Parker, J.C., Park, E., 2004. Modeling field-scale dense nonaqueous phase liquid dissolution kinetics in heterogeneous aquifers. Water Resour. Res. 40 (5).
Rao, P.S.C., Jawitz, J.W., Enfield, C.G., Falta Jr, R., Annable, M.D., Wood, A.L., 2001. Technology integration for contaminated site remediation: clean-up goals and performance criteria. Groundwater Qual. 275, 571–578.
Remy, N., Boucher, A., Wu, J., 2009. Applied Geostatistics with SGeMS: A User's Guide. Cambridge University Press.
Riva, M., Guadagnini, A., Fernandez-Garcia, D., Sanchez-Vila, X., Ptak, T., 2008. Relative importance of geostatistical and transport models in describing heavily tailed breakthrough curves at the Lauswiesen site. J. Contam. Hydrol. 101 (1), 1–13.
Riva, M., Guadagnini, L., Guadagnini, A., 2010. Effects of uncertainty of lithofacies, conductivity and porosity distributions on stochastic interpretations of a field scale tracer test. Stochast. Environ. Res. Risk Assess. 24 (7), 955–970.
Riva, M., Guadagnini, L., Guadagnini, A., Ptak, T., Martac, E., 2006. Probabilistic study of well capture zones distribution at the lauswiesen field site. J. Contam. Hydrol. 88 (1), 92–118.
Riva, M., Sanchez-Vila, X., Guadagnini, A., 2014. Estimation of spatial covariance of log conductivity from particle size data. Water Resour. Res. 50 (6), 5298–5308.
Rizzo, C.B., de Barros, F.P.J., 2017. Minimum hydraulic resistance and least resistance path in heterogeneous porous media. Water Resour. Res. 53 (10), 8596–8613.
Rubin, Y., 2003. Applied Stochastic Hydrogeology. Oxford University Press.
Salamon, P., Fernàndez-Garcia, D., Gómez-Hernández, J.J., 2006. A review and numerical assessment of the random walk particle tracking method. J. Contam. Hydrol. 87 (3–4), 277–305.
Scholz, C., Wirner, F., Götz, J., Rüde, U., Schröder-Turk, G.E., Mecke, K., Bechinger, C., 2012. Permeability of porous materials determined from the euler characteristic. Phys. Rev. Lett. 109 (26), 264504.
U.S. Environmental Protection Agency, 1989. Risk assessment guidance for superfund, Volume 1: Human health manual (Part A), Rep. EPA/540/1-89/002.
U.S. Environmental Protection Agency, 1997. Health Effects Assessment Summary Tables, FY1997 Update, Environ. Criteria and Assess. Off., Off. of Health and Environ. Assess., Off. of Res. and Dev., Cincinnati, Ohio.
U.S. Environmental Protection Agency, 1999. Anaerobic Biodegradation Rates of Organic Chemicals in Groundwater: A Summary of Field and Laboratory Studies. Off. of Solid Waste, Washington, D. C.
Warren, J.E., Skiba, F.F., et al., 1964. Macroscopic dispersion. Soc. Petroleum Eng. J. 4 (03), 215–230.
Zarlenga, A., de Barros, F.P.J., Fiori, A., 2016. Uncertainty quantification of adverse human health effects from continuously released contaminant sources in groundwater systems. J. Hydrol. 541, 850–861.